Author Manuscript

Author Manuscript

Author Manuscript

Author Manuscript

HHS Public Access

Author manuscript

Magn Reson Med. Author manuscript; available in PMC 2020 August 01.

Published in final edited form as:

Magn Reson Med. 2019 August ; 82(2): 706–720. doi:10.1002/mrm.27763.

Free Breathing Cine Imaging with Motion-Corrected Reconstruction at 3T Using SPiral Acquisition with Respiratory correction and Cardiac Self-gating (SPARCS)

Ruixi Zhou, MS[1], **Yang Yang, PhD**[2,3], **Roshin C. Mathew, MD**[2,4], **John P. Mugler III, PhD**[1,2,4], **Daniel S. Weller, PhD**[5], **Christopher M. Kramer, MD**[2,4], **Abdul Haseeb Ahmed, PhD**[6], **Mathews Jacob, PhD**[6], and **Michael Salerno, MD, PhD, MS**[1,2,4]

[1]Department of Biomedical Engineering, University of Virginia Health System

[2]Department of Medicine, Cardiovascular Division, University of Virginia Health System

[3]Translational and Molecular Imaging Institute and Department of Radiology, Icahn School of Medicine at Mount Sinai

[4]Radiology and Medical Imaging, University of Virginia Health System

[5]Department of Electrical and Computer Engineering, University of Virginia

[6]Department of Electrical and Computer Engineering, University of Iowa

Abstract

Purpose: To develop a continuous-acquisition cardiac self-gated spiral pulse sequence and a respiratory motion-compensated reconstruction strategy for free breathing cine imaging.

Methods: Cine data were acquired continuously on a 3T scanner for 8 seconds per slice without ECG gating or breath-holding, using a golden-angle gradient echo spiral pulse sequence. Cardiac motion information was extracted by applying principal component analysis on the gridded 8×8 *k*-space center data. Respiratory motion was corrected by rigid registration on each heartbeat. Images were reconstructed using a low rank and sparse (L+S) technique. This strategy was evaluated in 37 healthy subjects and 8 subjects undergoing clinical cardiac magnetic resonance (CMR) studies. Image quality was scored (1–5 scale) in a blinded fashion by two experienced cardiologists. In 13 subjects with whole heart coverage, left ventricular ejection fraction (LVEF) from SPARCS was compared to that from a standard ECG gated breath-hold balanced steady-state free precession (bSSFP) cine sequence.

Results: The self-gated signal was successfully extracted in all cases and demonstrated close agreement with the acquired ECG signal (mean bias −0.22 ms). The mean image score across all subjects was 4.0 for reconstruction using the L+S model. There was good agreement between the LVEF derived from SPARCS and the “gold-standard” bSSFP technique.

Corresponding Authors: Michael Salerno, MD, Ph.D., Director of Cardiac MRI, Associate Professor of Medicine, Radiology, and BME, Cardiovascular Division, University of Virginia Health System, 1215 Lee Street, PO Box 800158, Charlottesville, VA 22908, Phone: 434-243-7325, Fax: 434-982-1998, ms5pc@virginia.edu.

Author Manuscript Author Manuscript Author Manuscript Author Manuscript

Conclusions: SPARCS successfully images cardiac function without the need for ECG gating or breath-holding. With an 8-second data acquisition per slice, whole heart cine images with clinically acceptable spatial and temporal resolution and image quality can be acquired in less than 90 seconds of free-breathing acquisition.

Keywords

Cardiac MRI; spiral trajectory; golden angle; self-gating; motion correction; low-rank and sparse

Introduction

Cardiac magnetic resonance cine imaging is widely regarded as the “gold-standard” technique for the non-invasive assessment of cardiac function. Typically, images are acquired using breath-held 2D segmented ECG-gated balanced steady-state free precession (bSSFP) pulse sequences. The approach of using ECG triggering and breath-hold acquisition has several limitations. Firstly, the ECG signal can be distorted, particularly at higher field strengths (3T), due to the magnetohydrodynamic effect (1), rapid switch of magnetic-field gradients (2), as well as radiofrequency interference (3,4) resulting in mis-triggering. Furthermore, optimal placement of the ECG leads increases the time to prepare the patient for the CMR exam. Additionally, a significant number of patients are not able to adequately hold their breath during cine acquisition, resulting in motion artifacts and the need to repeat image acquisition of the same slice location on subsequent breath-holds. Even if the patient can perform good breath-holds, this approach is inefficient as it requires 10–12 breath-holds to cover the left ventricle (LV), which can take longer than 10 minutes, and requires coordination between the operator and the patient. Real-time imaging techniques, which do not require ECG gating or breath-holding can be used clinically; however, some of these techniques may sacrifice spatial and/or temporal resolution (5–7). Thus, there is a growing interest in free-breathing and self-gated approaches that can acquire images with excellent quality that have high temporal and spatial resolution.

A number of methods have been used to enable ECG-gated free breathing cine examinations. Diaphragmatic navigator-echo based methods have been used to track respiratory motion (8–11). However, they typically preclude retrospective ECG gating, and the total scanning time is prolonged depending on respiratory gating efficiency. Projection navigators acquired during bSSFP acquisitions have been successfully utilized to perform respiratory tracking without the need for a separate diaphragmatic navigator (12), but this approach is still limited by navigator gating efficiency. Recent studies (13–18) have used the acquired data itself to derive the respiratory gating signal. Data were then separated into different respiratory states (16,19,20) and reconstruction was performed using data from a subset of the respiratory states, or by using motion correction to combine data from different respiratory states.

Cardiac “self-gated” techniques (21,22) have been proposed to eliminate the need for ECG synchronization by acquiring and processing additional MR signals to derive cardiac cycle timing information resulting in decreased imaging efficiency. These studies have extracted the cardiac “self-gating” signal from the acquired data during breath-holds (23–25) or free-

Author Manuscript Author Manuscript Author Manuscript Author Manuscript

breathing (19,20,26). Previously reported cardiac self-gating approaches have used the *k*-space center point (22,27) or center *k*-space line (5,13,14,23) as navigator signals. Some techniques (23,28) also used image-based methods to obtain self-gating signals.

In terms of sampling strategy, most studies have utilized Cartesian or radial trajectories (13–15,21–23,28). Spiral acquisitions are more time efficient than Cartesian or radial acquisitions as they cover a greater extent of *k*-space each repetition time (TR). The TR for spiral cardiac imaging at 3T can be twice as long as that used for Cartesian or radial imaging resulting in an increase of the flip angle that can be used, thus providing a signal-to-noise (SNR) advantage. Assuming a T1 of myocardium of 1200 ms, an increase in the TR from 4–5 ms to 8 ms would increase the Ernst angle by 25–40%. Increasing the flip angle results in a corresponding increase in SNR. This increased TR also allows for more time for inflow of unsaturated blood as compared to other acquisition strategies. The enhanced inflow effect should also result in high SNR for the blood-pool and higher blood-myocardial contrast-to-noise (CNR) (29). Because each spiral interleaf starts from the center of *k*-space, spiral imaging is also robust to flow and motion artifacts (7). Taking advantage of these properties of a spiral acquisition which fully samples the center of *k*-space on each interleaf, self-gating can be performed without any need for additional navigator lines or projections. A recent study has used a breath-held cardiac self-gated spiral technique to quantify coronary artery vasodilation (25). To date, no studies have explored the use of free-breathing cardiac and respiratory self-gated golden angle spiral trajectories for the evaluation of cardiac anatomy and function.

Despite a number of recent advances, there are still several limitations to be overcome. Firstly, for imaging at 3T, bSSFP sequences typically require frequency-scouts and careful shimming to avoid off-resonance artifacts such as banding artifact and thus may be less robust for automatic free breathing acquisition. To address this issue, our SPiral Acquisition with Respiratory correction and Cardiac Self-gating (SPARCS) utilized a gradient echo pulse sequence (GRE) with data acquired using a single spiral interleaf rotated by the golden-angle (137.51°) in time. While spiral pulse sequences are sensitive to blurring from off-resonance, short spiral readout durations can be used to mitigate this issue. Self-gating approaches usually require careful selection of receive coil elements to obtain self-gating signals as each coil has different sensitivity to cardiac motion and respiratory motion. Here, the cardiac self-gating signal was extracted using principal component analysis (PCA) on a gridded 8×8 central region of *k*-space for each spiral, which eliminates the process of selecting coils that contribute significant aliasing artifacts in the heart region. This also improves the performance of coil compression and image reconstruction. Finally, as it is inefficient to discard data acquired at different respiratory phases, we utilized rigid registration of the data from each heartbeat to correct the breathing motion to obtain 100% data acquisition efficiency. Images were reconstructed with a rigid-motion compensated low rank and sparse (L+S) technique (30). SPARCS was designed to provide whole heart coverage with clinically relevant spatial (1.25 mm × 1.25 mm) and temporal (< 40 ms) resolution from a self-gated free breathing acquisition of less than 90 seconds.

Author Manuscript Author Manuscript Author Manuscript Author Manuscript

Methods

Cardiac Self-Gating Strategy

The automatic pipeline that we developed for cardiac self-gating is shown in Figure 1. Self-gating cardiac signals were determined by gridding an 8×8 fully sampled central region of *k*-space for each spiral interleaf for all receiver coils (Figure 1(a)), followed by low-pass temporal filtering to eliminate the high frequency component caused by the golden-angle sampling pattern. Next, PCA was performed on this data. The first 5 temporal-basis functions, which typically explained greater than 90% of total variance, were used for further processing (Figure 1(b)). To extract and determine the cardiac self-gating signal, a band-pass filter with a passband from 0.5 Hz to 2 Hz was applied to the 5 temporal-basis functions. Then, frequency spectrum analysis was used to find the cardiac motion-related component by determining which basis function had the highest amplitude in the cardiac motion frequency range (Figure 1(c)). Finally, the cardiac self-gating triggers were extracted by performing peak detection on this filtered temporal-basis function. To exclude potential artifactual peaks that are unrelated to cardiac motion, a signal threshold was set by taking the mean of all the peaks and troughs (Figure 1(d)). Since the cardiac trigger from self-gating signal is based on the *k*-space center intensity, rather than on the physiological ECG signal, the triggers derived from SPARCS are typically not at the same time as the triggers derived from an ECG signal, as shown in Supporting Information Figure S1. However, as the signal fluctuation varies reproducibly between systole and diastole, the SPARCS gating signal is consistent from beat to beat. Thus, the R-R interval of the SPARCS gating signal and the ECG signal were very similar. As the heart shape varies between different slices the exact position of the trigger within the cardiac cycle may be different at the different slice locations. To compare gating data across all subjects and slice positions, we compared the recorded ECG R-R interval length versus the cardiac cycle length as determined by the time interval between subsequent SPARCS triggers. When determining ejection fraction (EF), end-diastole and end-systole were determined visually for each slice, and the images from each slice were aligned. This is a limitation of all non-ECG gated techniques including non-gated free breathing techniques. A respiratory gating signal can also be obtained from the PCA data using a band-pass filter with a frequency range from 0.05 Hz to 0.5 Hz (Figure 1(e)). While in SPARCS we use registration to correct for respiratory motion, this PCA respiratory gating signal, or the displacements derived from registration, could be used for self-gating to reject data that is outside of a desired “self-gating” window.

Once the cardiac triggers were detected, the data were retrospectively binned to a fixed number of phases across the cardiac cycle. This number of phases was determined by dividing the average cardiac trigger interval (cardiac cycle length) by a fixed temporal resolution of 39 ms, corresponding to 5 spiral interleaves (Figure 2(a)). This resulted in 25–35 cardiac phases depending on the average length of the cardiac cycle.

Respiratory Motion Correction

We developed a fully automated strategy (31) to detect an 80×80 pixel region of interest (ROI) containing the heart. Using a Non-Uniform Fast Fourier Transform (NUFFT) reconstruction (32) of the retrospectively binned cardiac data, the heart was detected

Author Manuscript Author Manuscript Author Manuscript Author Manuscript

automatically based on the fact that, in cine imaging, the heart region has the largest magnitude changes in signal intensity due to cardiac motion. Thus, the ROI containing the heart was automatically detected by finding the largest connected region of high standard deviation on a standard deviation map, whose signal intensity was calculated from the whole dynamic dataset (Figure 2(a)).

To correct the respiratory motion, it was assumed that the respiratory position does not vary considerably during each R-R interval. Based on this assumption, the *k*-space data over each R-R interval was combined to create a static image for each heartbeat (Figure 2(b)). Rigid registration was performed over the heart ROI to determine the in-plane displacements required to compensate for the bulk changes in heart position resulting from respiratory motion. While breathing results in non-rigid motion of structures of the chest, the motion of a small square ROI around the heart on a cardiac gated short-axis image can be reasonably approximated by in-plane rigid motion in the head-foot and anterior-posterior directions (31). Rigid translational registration was performed by using mutual information as a metric to determine the rigid transformation from the source image to that of the target image (33) (Figure 2(b)). Images from all frames were first registered to the image from the first acquired heartbeat to derive the relative displacements due to respiratory motion. The end-expiration state image was then determined by finding the most positive head-foot and anterior-posterior shift along the curve. The displacement information was adjusted by treating the end-expiration image as the target image, and this displacement was used to derive the appropriate *k*-space linear phase shifts to register the heart. The difference between registering the images to end-inspiration and to end-expiration can be appreciated in Supporting Information Figure S2. These linear phase shifts derived from each R-R interval combined images were applied to the acquired raw *k*-space data for each frame within that R-R interval as previously described (31).

Image Reconstruction

Unlike in Cartesian imaging where the aliasing manifests as wrapping in the phase encoding direction, for spiral imaging aliasing appears as swirling artifacts on the opposite side of the unsupported portion of the field of view (FOV), which could affect image quality within the heart region. Therefore, we developed a strategy to automatically select coils based on a spiral aliasing artifact ratio within the automatically detected heart ROI (Figure 2(c)). Our method was inspired by several studies (34,35) that have developed techniques for automatic coil selection to reduce streaking artifacts in radial acquisitions. By using golden-angle sampling, increasing the temporal window for reconstruction results in an increase in the supported FOV such that a completely unaliased image (Ref_{heart}) can be recovered. By comparing this to an image that does not support the whole FOV (i.e. smaller temporal window, Img_{heart}), we can characterize the aliasing pattern and assess its impact on the desired FOV. An artifact ratio was defined over the heart ROI for the k^{th} coil (r_k) as:

$$r_k = \frac{\left\| Ref_{heart}(k) - const \times Img_{heart}(k) \right\|_F}{\left\| Ref_{heart}(k) \right\|_F}, \qquad k \in [1, N] \quad \text{(Eq. 1)}$$

Author Manuscript Author Manuscript Author Manuscript Author Manuscript

where N is the number of coils, Ref_{heart} is an aliasing-free multi-coil magnitude (reference) image that was reconstructed by using 100 continuous-acquired spirals, Img_{heart} indicates an under-sampled multi-coil magnitude image with aliasing artifacts reconstructed using only 30 spirals, and *const* is a constant value calculated based on the energy difference of the reference and aliasing images, which is the ratio between the number of spirals that were used to generate the reference and under-sampled images. $\|*\|_F$ indicates the Frobenius-norm. To eliminate coils which predominantly contribute aliasing artifacts over the heart region, while still having an adequate number of coils for parallel imaging, coils with an artifact ratio lower than 0.3 were retained. This threshold was chosen by screening the selection of coils in 10 subjects. After coil selection, we used PCA-based coil compression to decrease the number of coils to reduce computations during reconstruction.

Images were reconstructed using low rank and sparse decomposition (30) as follows:

$$\min_{L,S} \frac{1}{2}\|E(L+S)-d\|_2^2 + \lambda_L\|L\|_* + \lambda_S\|TS\|_1 \quad \text{(Eq. 2)}$$

where E is the encoding operator, d is the under-sampled k-space data, L and S are space-time matrices corresponding to low rank and sparse representations respectively, T is a sparsifying transform, and λ_L and λ_S are coefficients to trade off the weight of data consistency for the low rank and sparse terms. Temporal finite difference was used as the sparsifying transform. This method can reconstruct highly accelerated dynamic MRI datasets by separating the background static-information from the dynamic information. In the reconstruction, the iterative SENSE algorithm (36) was adopted to enforce joint multi-coil low rank (L) and sparsity (S) simultaneously to exploit inter-coil correlations. Data compression in the L model was performed by truncating the singular value decomposition (SVD) representation of the dynamic image series while in the S model it was done by discarding low-value coefficients in the temporal total variation domain. Coil sensitivity maps were computed from the temporal average of binned data using the adaptive coil combination technique (37). Reconstruction parameters were chosen based on providing images with adequate reduction in aliasing artifacts with minimal visual temporal blurring of the endocardial border. To determine appropriate values for λ_L and λ_S, SPARCS cine data from 3 subjects were reconstructed with λ_L and λ_S varied over a range from 0.000001 to 0.1. An experienced cardiologist chose the combination of λ_L and λ_S which resulted in images with reduced aliasing artifacts and no obvious temporal blurring. The parameters λ_L of 0.01 and λ_S of 0.00001 were chosen and used to reconstruct all datasets. Data were also reconstructed using kt-SLR (38) following similar methodology for selection of regularization parameters.

Human Imaging

Continuous spiral cine imaging was performed in 45 subjects. The subjects included 37 healthy volunteers and 8 patients undergoing clinical CMR studies. Written informed consent was obtained from all subjects, and imaging studies were performed under institutional review board (IRB) approved protocols. Scanning was performed on a 3T scanner (MAGNETOM Prisma or Skyra, Siemens Healthineers, Erlangen, Germany) at the

Author Manuscript Author Manuscript Author Manuscript Author Manuscript

University of Virginia Medical Center. Image datasets were acquired using the standard body phased-array RF coil. Pulse sequence parameters included: FOV = 320 mm, TR = 7.8 ms, TE = 1 ms, voxel size = 1.25×1.25 mm^2, slice thickness = 8 mm, flip angle = 15°. A dual density (DD) spiral readout trajectory was rotated by the golden angle between subsequent TRs for data acquisition. The DD spiral had a fermi-function transition region with a *k*-space density of 0.2 times Nyquist for the first 20% of the trajectory and an ending density of 0.02 times Nyquist (39). This density was chosen such that the center of *k*-space would be approximately fully sampled and the outer-region of *k*-space would have a maximum acceleration factor of approximately 8x for the combination of 5 spiral interleaves (39 ms temporal resolution). Data were acquired for 8 seconds per slice.

For 32 subjects, continuously acquired spiral data were obtained at a single short-axis location. During the acquisition, the ECG signal was also recorded. The R-R interval length from the ECG signal and extracted cardiac trigger from SPARCS were compared using Bland-Altman (40) and linear regression plots. Images were reconstructed from 8 seconds worth of data (1000 spirals) using NUFFT and L+S techniques. The first 200 spirals in the acquired data were discarded to allow the signal to achieve steady state. To evaluate quantification of LVEF, slices covering the whole heart in short-axis were collected in 13 subjects including: 10 healthy volunteers and 3 clinical subjects. EF was determined by manual tracing of the endocardial borders by an experienced cardiologist. The calculated LVEF was compared to that from the standard clinical breath-hold ECG gated bSSFP sequence.

Image quality for all datasets was assessed by 2 experienced cardiologists blinded to the reconstruction technique. Image quality was evaluated on a 5-point scale ranging from 1 (poor and not usable) to 5 (clinically excellent). A score of 3 would be clinically acceptable, but with some artifacts. Comparison between the scores from the different techniques were compared using Friedman's test and Wilcoxon signed-rank tests for the comparisons between individual reconstruction techniques. The EF comparison between the techniques was performed using a two-way ANOVA analysis with Tukey's Studentized Range test to correct for multiple comparisons. Statistical analysis was performed using SAS software 9.4 (SAS Institute Inc., Cary, NC).

Results

Cardiac Self-Gating

R-R interval length was compared between the recorded ECG signals and the extracted cardiac "self-gated" trigger signals as shown in Figure 3. The mean difference between the ECG and self-gating cardiac cycle lengths for the patients with measured ECG data was −0.22 ms, with a 95% confidence interval of 61.95 ms to −62.38 ms. There was a good correlation, $R^2 = 0.96$, between the R-R interval length from ECG and self-gated cardiac signals without a significant bias (p = 0.92, paired sample *t* test).

As the self-gated cardiac trigger and ECG signals performed similarly, the self-gating strategy provides a reasonable surrogate. While ECG gating techniques have improved

Author Manuscript Author Manuscript Author Manuscript Author Manuscript

significantly, ECG gating can sometimes be unreliable at 3T, particularly in patients with high BMI (as shown in Supporting Information Figure S3 and Video S1).

Respiratory Motion Correction

Figure 4 shows the rigid registration performance from one representative subject. After the heart region was automatically detected (Figure 4(a)), images from each self-gated cardiac interval were registered to correct for respiratory motion. The anterior-posterior (x) and head-foot (y) displacements extracted from rigid registration are plotted in Figure 4(b). The registration performance can be seen by comparing the x-t and y-t (Figure 4(d)) profiles before and after rigid registration, where the crossing lines on x and y directions are shown in Figure 4(c). After registration, both x-t and y-t profiles (Figure 4(d)) are sharper and less corrupted by respiratory motion.

Evaluation of Cine Images

Figure 5 demonstrates the automatic coil selection results. Coil images in a region around the heart are shown in Supporting Information Figure S4. As expected, the coils that have a high SNR and low aliasing in the heart region rank higher. With a threshold of artifact energy of 0.3, coils whose images are circled in green were retained while the ones in red were discarded. Figure 5(a) and 5(b) show the NUFFT image results before and after automatic coil selection, respectively. The difference image of these is shown in Figure 5(c), with a 10-fold scaling factor. In this particular case, the aliasing artifacts caused by remote coils started from the bottom right (red arrow) and extended all the way into the heart region. Automatic coil selection significantly reduced aliasing artifacts.

Figure 6 shows reconstructed short-axis cine images from a healthy volunteer. The first row (Figure 6(a-c)) shows cine images reconstructed with NUFFT while the second row (Figure 6(d-f)) shows the L+S reconstructed images. The third row (Figure 6(g-i)) shows the clinically used breath-hold ECG-gated bSSFP images. End-diastolic and end-systolic images are shown in the first and second columns respectively. X-t profiles for the reconstructed images along the profile denoted by the dashed line in Figures 6(a), (d) and (g) show preserved temporal fidelity of the SPARCS technique. Figure 7 demonstrates images from a subject in the patient group. In this clinical subject, mild susceptibility artifacts are seen in the bSSFP images (indicated by red arrows) in Figure 7(g-i). As the NUFFT technique reconstructs each frame independently, it is free of temporal blurring between frames, but less effective at reducing aliasing artifacts (e.g., red arrows in Figure 6) as compared to the L +S reconstruction. The difference in image quality can be more easily appreciated in Supporting Information Videos S2 and S3. The X-t profiles from the L+S reconstruction show the reduction of residual aliasing artifacts without introducing significant visual temporal blurring as compared to NUFFT.

Image-quality scores (N = 42) from the 2 cardiologists are shown in Figure 8. Here, the 3 subjects that were used to tune L+S reconstruction parameters were excluded. The mean (± standard deviation) image-quality scores of SPARCS NUFFT, SPARCS L+S and breath-hold ECG-gated bSSFP images were 3.2 (± 0.7), 4.0 (± 0.7) and 4.5 (± 0.6). The L+S reconstruction was graded significantly higher than the SPARCS NUFFT reconstruction ($p <$

Author Manuscript Author Manuscript Author Manuscript Author Manuscript

0.001), and breath-hold ECG-gated bSSFP was graded significantly higher than SPARCS NUFFT and L+S reconstruction ($p < 0.001$). SPARCS images with kt-SLR reconstruction performed similar to SPARCS with L+S reconstruction (Supporting Information Figure S5, Videos S2, S3). Given the relatively short readout duration per interleaf, the SPARCS images had minimal blurring or signal dropout artifacts due to off-resonance. Fine trabeculations were clearly visualized in the right and left ventricles in the SPARCS images.

Figure 9 shows the L+S reconstructed images from one subject with 10 slices covering the left ventricle. Figure 9(a) corresponds to end-diastolic frames and Figure 9(b) are end-systolic frame images. Movies of a subject's whole-heart coverage using L+S reconstruction are shown in the Supporting Information Video S4. Across all studies with whole ventricular data (N = 13), the mean (± standard deviation) LVEF for NUFFT and L+S were 58.5 (± 7.6) and 57.3 (± 7.9), respectively, for the SPARCS technique as compared to 58.3 (± 7.7) for the standard bSSFP cine images. A Bland-Altman plot comparing EF between Cartesian bSSFP images and SPARCS NUFFT spiral images is shown in Figure 10(a), and one comparing Cartesian bSSFP images and SPARCS L+S spiral images is shown in Figure 10(b). A blocked ANOVA test showed no significant difference among the 3 groups ($p = 0.09$), demonstrating the accuracy of calculating LVEF using the proposed SPARCS strategy.

Discussion

In this work a free-breathing, continuous-acquisition, respiratory and cardiac self-gated, golden-angle spiral-cine strategy (SPARCS) was proposed and developed. The method used the 8×8 *k*-space center region from the acquired data to derive a cardiac trigger signal without the need for ECG gating.

To enable free-breathing acquisition with 100% sampling efficiency, a rigid registration strategy was implemented to correct respiratory motion between heartbeats. While currently there are more complex techniques for non-rigid registration(41,42), their performance is sensitive to image quality related factors, and their implementation for non-Cartesian trajectories significantly increases reconstruction time and complexity. Since most cardiac motion caused by breathing is in the head-foot and anterior-posterior directions, a rigid registration can be used. We have previously demonstrated the robustness of this motion-correction strategy for myocardial perfusion imaging (31).

As SPARCS registers data acquired at different respiratory phases, residual uncorrected respiratory motion could cause some loss of spatial resolution. This is true of all techniques which achieve 100% navigator efficiency using registration. Our approach assumes that respiratory motion within each heartbeat is relatively small. The difference in respiratory position in the head-foot direction between beats across all subjects typically fell within a ± 2–4 mm window, which is in the range of typical diaphragmatic navigator acceptance windows of 4–8 mm (10,43). Correction of residual respiratory motion with each heartbeat may be feasible using a sliding window approach to assess the respiratory position throughout the cardiac cycle. However, such an algorithm would have to account for changes in the heart position due to cardiac contraction and would add additional complexity to the reconstruction. Blurring due to residual respiratory motion could be a disadvantage of self-

Author Manuscript Author Manuscript Author Manuscript Author Manuscript

gating techniques as compared to real-time techniques and requires further investigation. This strategy also does not account for through-plane motion or potential differences in cardiac morphology between inspiration and expiration. As the respiratory phase of each heartbeat is known, discordant data could be rejected either using a self-gating window as we have used for free-breathing T1 mapping (44), or based on an image correlation metric as has been used for free-breathing LGE imaging (45). The trade-off for rejecting data would be a reduction in acquisition efficiency. As the R-R interval duration for each heartbeat is also known, heartbeats with significantly different durations can also be rejected, again at the cost of acquisition efficiency.

At relatively low acceleration factors (2–3x), non-Cartesian SPIRiT (46) and non-Cartesian SENSE (47) perform well for spiral imaging. For more highly accelerated spiral techniques, compressed sensing approaches have been shown to improve reconstruction performance (39). The L+S reconstruction method can provide a decomposition of low rank and sparsity components to separate background and dynamic components in an image. The L component captures static and periodic motion in the background among cardiac phases, while the S component contains the dynamic cardiac motion information. Since the background has been suppressed, the S component has a sparser representation than the original matrix (30). By exploiting the spatial and temporal correlation of the dynamic image series with an iterative SENSE implementation, the L+S method offers an efficient and robust reconstruction. L+S reconstruction with inappropriate regularization parameters could suffer from temporal blurring. We chose the smallest regularization parameters for the L+S reconstruction that visually reduced spatial blurring without obvious loss of temporal fidelity. Furthermore, we intentionally compared L+S to NUFFT so that we could directly assess the effects of temporal regularization on the temporal fidelity of the L+S reconstruction. Our assessment of LVEF with L+S reconstruction as compared to NUFFT reconstruction of the SPARCS data and the breath-held cine bSSFP data demonstrates that the respiratory motion correction and temporal regularization do not result in significant biases in determination of the LVEF. This is important as LVEF remains a key parameter for clinical decision making. However, we note that some reduction in spatial resolution due to residual respiratory motion may not greatly impact the measured EF. Other reconstruction techniques, such as kt-SLR could also be used with the SPARCS self-gating and respiratory motion correction framework (Supporting Information Videos S2 and S3). The comparison of EF measurements between SPARCS and the “gold-standard” Cartesian method had no significant bias, and clinically acceptable limits of agreement. Prior studies (48,49) have demonstrated similar limits of agreement for intra-observer, inter-study EF measurements as −5.19 to 6.33.

Although bSSFP sequences are typically used for cine imaging due to improved contrast to noise ratio, a gradient echo strategy may have advantages for simplifying 3T cine imaging. As the spiral-trajectory implementation has a relatively long TR, there is more time for inflow-enhancement of the LV blood pool resulting in a contrast which is similar to Cartesian bSSFP imaging rather than that seen with short-TR Cartesian GRE imaging. As the sequence is spoiled GRE-based rather than SSFP-based, a frequency scout, which is often needed for bSSFP acquisition to avoid banding artifacts and out of plane flow artifacts, is not required. While spiral techniques may be sensitive to off-resonance artifacts, for cine

Author Manuscript Author Manuscript Author Manuscript Author Manuscript

applications at 3T we have found that a readout duration of 5 ms or less produces acceptable results without off-resonance correction. The SPARCS technique is compatible with off-resonance deblurring techniques (50), and spectral-spatial excitation (51) could be used to further eliminate the signal from fat. With 8 seconds of data acquisition per slice, the whole ventricle can be covered in about 90 seconds. The approach described in this manuscript could potentially also be applied to spiral bSSFP imaging at 1.5T (7) or 3T.

The idea of self-navigation was first pioneered by Larson et al. (23) for cardiac cine imaging using radial *k*-space sampling and a breath-hold SSFP sequence, where the self-gated signal was extracted from the echo-peak magnitude, kymogram and 2D correlation. This idea was further explored by using the center *k*-space point (22), center *k*-space line (5) or processed center *k*-space data (25). These cardiac "self-gated" methods typically use breath holds to avoid the complexity of separating cardiac motion and respiratory motion. Some studies also focused on free breathing imaging using navigator signals (16,17,52). A respiratory and cardiac self-gated method using a multi-echo 3D hybrid radial SSFP acquisition strategy was proposed by Liu et al. (19), where coils were selected based on the smallest variance of either the R-R intervals or respiratory positions for each individual coil. In our technique, PCA is used to separate combinations of coils which correspond predominantly to the respiratory and cardiac signals. The optimal PCA basis functions for the cardiac and respiratory self-gating signal were determined by choosing the basis functions which had the highest amplitude in the cardiac or respiratory frequency ranges after band-pass filtering. Another study by Pang et al. (17) retrospectively binned the data into different cardiac and respiratory phases based on information extracted from self-gated projections, and the different respiratory states were reconstructed to perform motion correction. This approach could have potential issues with subjects that have irregular breathing patterns resulting in some respiratory bins with not enough data to reconstruct a reasonable quality image to do motion correction between bins. Thus, the performance of binning the data into different respiratory bins might vary in individuals with different breathing patterns. In the proposed SPARCS method, respiratory motion was corrected for each R-R interval, which should provide robustness to irregular breathing patterns. SPARCS provides cine images with similar spatial and temporal resolution to current clinical breath-hold techniques with a short free-breathing self-gated acquisition. In the future this technique could be compared to other free-breathing and/or self-gated techniques.

While previous real-time techniques required a sacrifice of spatial and/or temporal resolution, newer real-time techniques, such as real-time compressed sensing (CS) cine imaging, are becoming clinically available and are demonstrating real-time imaging with high spatial and temporal resolution. The current clinically available real-time compressed-sensing technique still requires an ECG to define the R-R interval (53), and the manufacturer recommends that this real-time technique is performed during a breath-hold. The L+S model we used in SPARCS is similar to the real-time CS reconstruction. Unfortunately, we could not compare SPARCS directly to this real-time CS technique, as it was not available on our scanner. A future comparison between SPARCS and such techniques is warranted.

There are also several limitations for the current SPARCS strategy. Firstly, the spiral based acquisitions may be more sensitive to off-resonance artifacts than Cartesian GRE.

Author Manuscript Author Manuscript Author Manuscript Author Manuscript

Nonetheless, with short spiral readouts, there is relatively little spiral-induced blurring or dropout artifacts. Additionally, off-resonance correction can be applied to further improve off-resonance performance. GRE based acquisitions have lower CNR and SNR as compared to SSFP techniques. This is partially compensated for in the SPARCS technique by using a longer TR and higher flip angles. Our group has previously demonstrated that SSFP-based spiral imaging is also feasible at 1.5T and a prior study showed it could be performed at 3T (54). Compared with the ECG signal trigger, which always corresponds to the beginning of systole, the SPARCS extracted cardiac trigger can vary within the cardiac cycle. Moreover, this technique involves binning of data and could be sensitive to arrhythmias. To overcome this issue, data from R-R intervals that differ significantly from the mean R-R interval can be rejected, and data acquisition time could be extended if needed. Our filter cut-off frequency was set to support a maximum heart rate of 120 bpm. For all subjects scanned, the maximum heart rate was < 120 bpm, which justified a filter cutoff frequency of 2 Hz as reasonable when extracting the cardiac trigger. However, in pediatric patients or other patients with high heart rates, increasing the cutoff frequency to 3 Hz would support maximum heart rates of 180 bpm. The current computation times to run the SPARCS pipeline using unoptimized MATLAB (The Mathworks Inc., Natick, MA) code with NUFFT or L+S reconstruction is 3 minutes or 6 minutes per slice, respectively, using a 2.4-GHz 8-core Intel Xeon CPU and 128 GB of RAM. The reconstruction time can be further improved by implementing the reconstruction in C++ and utilizing GPUs.

To summarize, the SPARCS technique can obtain 2D cine images with clinically acceptable spatial and temporal resolution, and adequate image quality, in a short free-breathing self-gated acquisition. In the future, this idea can be extended to a 3D or simultaneous multi-slice (SMS) acquisition. Although it might result in reduced contrast between the blood-pool and myocardium, an approach similar to that used for GRE-based coronary angiography at 3T, where images were acquired after administration of contrast, could also be utilized.

Conclusions

A free-breathing, continuous-acquisition, respiratory and cardiac self-gated, golden-angle spiral-cine imaging strategy, SPARCS, was presented. It enables cardiac cine imaging without ECG leads and with free breathing, which provides a simpler and more efficient protocol for clinical CMR imaging.

Supplementary Material

Refer to Web version on PubMed Central for supplementary material.

Acknowledgements

The authors would like to acknowledge the help of our study coordinators and nurses Jayne Missel RN, Jennifer Kay RN, and Caroline Flournoy PhD, and our research CMR technologists Jose M. Reyes, RT(R)MR and Joseph Hylton, RT(R)MR.

Funding Sources: NIH K23 HL112910, NIH R01 HL131919, Wallace H. Coulter Foundation Grant

Author Manuscript Author Manuscript Author Manuscript Author Manuscript

Reference

1. Keltner JR, Roos MS, Brakeman PR, Budinger TF. Magnetohydrodynamics of blood flow. Magn. Reson. Med 1990;16:139–149. doi: 10.1002/mrm.1910160113. [PubMed: 2255234]
2. Polson MJR, Barker AT, Gardiner S. The effect of rapid rise-time magnetic fields on the ECG of the rat. Clin. Phys. Physiol. Meas 1982;3:231–234. doi: 10.1088/0143-0815/3/3/008. [PubMed: 7140162]
3. Shetty AN. Suppression of Radiofrequency Interference in Cardiac Gated MRI: A Simple Design. Magn. Reson. Med 1988;8:84–88. [PubMed: 3173072]
4. Damji AA, Snyder RE, Ellinger DC, Witkowski FX, Allen PS. RF interference suppression in a cardiac synchronization system operating in a high magnetic field NMR imaging system. Magn. Reson. Imaging 1988;6:637–640. doi: 10.1016/0730-725X(88)90086-0. [PubMed: 3210907]
5. Uribe S, Muthurangu V, Boubertakh R, Schaeffter T, Razavi R, Hill DLG, Hansen MS. Whole-heart cine MRI using real-time respiratory self-gating. Magn. Reson. Med 2007;57:606–613. doi: 10.1002/mrm.21156. [PubMed: 17326164]
6. Uribe S, Beerbaum P, Sørensen TS, Rasmusson A, Razavi R, Schaeffter T. Four-dimensional (4D) flow of the whole heart and great vessels using real-time respiratory self-gating. Magn. Reson. Med 2009;62:984–992. doi: 10.1002/mrm.22090. [PubMed: 19672940]
7. Feng X, Salerno M, Kramer CM, Meyer CH. Non-Cartesian balanced steady-state free precession pulse sequences for real-time cardiac MRI. Magn. Reson. Med 2016;75:1546–1555. doi: 10.1002/mrm.25738. [PubMed: 25960254]
8. Firmin D, Keegan J. Navigator echoes in cardiac magnetic resonance. J. Cardiovasc. Magn. Reson 2001;3:183–193. doi: 10.1081/JCMR-100107467. [PubMed: 11816615]
9. Jung B, Zaitsev M, Hennig J, Markl M. Navigator gated high temporal resolution tissue phase mapping of myocardial motion. Magn. Reson. Med 2006;55:937–942. doi: 10.1002/mrm.20808. [PubMed: 16450375]
10. Peters DC, Nezafat R, Eggers H, Stehning C, Manning WJ. 2D free-breathing dual navigator-gated cardiac function validated against the 2D breath-hold acquisition. J. Magn. Reson. Imaging 2008;28:773–777. doi: 10.1002/jmri.21417. [PubMed: 18777547]
11. Abd-Elmoniem KZ, Obele CC, Sibley CT, Matta JR, Pettigrew RI, Gharib AM. Free Breathing Single Navigator Gated Cine Cardiac Magnetic Resonance at 3 Tesla: Feasibility Study in Patients. J Comput Assist Tomogr 2011;35:382–386. doi: 10.1097/RCT.0b013e31821b0ade.Free. [PubMed: 21586935]
12. Moghari MH, Barthur A, Amaral ME, Geva T, Powell AJ. Free-breathing whole-heart 3D cine magnetic resonance imaging with prospective respiratory motion compensation. Magn. Reson. Med. [Internet] 2017;189:181–189. doi: 10.1002/mrm.27021.
13. Stehning C, Bornert P, Nehrke K, Eggers H, Stuber M. Free-breathing whole-heart coronary MRA with 3D radial SSFP and self-navigated image reconstruction. Magn. Reson. Med 2005;54:476–480. doi: 10.1002/mrm.20557. [PubMed: 16032682]
14. Lai P, Bi X, Jerecic R, Li D. A Dual-Projection Respiratory Self-Gating Technique for Whole-Heart Coronary MRA. Magn. Reson. Med 2009;62:731–738. doi: 10.1002/mrm.22058. [PubMed: 19526514]
15. Lai P, Bi X, Jerecic R, Li D. A respiratory self-gating technique with 3D-translation compensation for free-breathing whole-heart coronary MRA. Magn. Reson. Med 2009;62:731–738. doi: 10.1002/mrm.22058. [PubMed: 19526514]
16. Usman M, Atkinson D, Odille F, Kolbitsch C, Vaillant G, Schaeffter T, Batchelor PG, Prieto C. Motion corrected compressed sensing for free-breathing dynamic cardiac MRI. Magn. Reson. Med 2013;70:504–516. doi: 10.1002/mrm.24463. [PubMed: 22899104]
17. Pang J, Bhat H, Sharif B, Fan Z, Thomson LEJ, Labounty T, Friedman JD, Min J, Berman DS, Li D. Whole-heart coronary MRA with 100% respiratory gating efficiency: Self-navigated three-dimensional retrospective image-based motion correction (TRIM). Magn. Reson. Med 2014;71:67–74. doi: 10.1002/mrm.24628. [PubMed: 23401157]

Author Manuscript Author Manuscript Author Manuscript Author Manuscript

18. Usman M, Ruijsink B, Nazir MS, Cruz G, Prieto C. Free breathing whole-heart 3D CINE MRI with self-gated Cartesian trajectory. Magn. Reson. Imaging 2017;38:129–137. doi: 10.1016/j.mri.2016.12.021. [PubMed: 28034638]
19. Liu J, Spincemaille P, Codella NCF, Nguyen TD, Prince MR, Wang Y. Respiratory and cardiac self-gated free-breathing cardiac CINE imaging with multiecho 3D hybrid radial SSFP acquisition. Magn. Reson. Med 2010;63:1230–1237. doi: 10.1002/mrm.22306. [PubMed: 20432294]
20. Pang J, Sharif B, Fan Z, Bi X, Arsanjani R, Berman DS, Li D. ECG and navigator-free four-dimensional whole-heart coronary MRA for simultaneous visualization of cardiac anatomy and function. Magn. Reson. Med 2014;72:1208–1217. doi: 10.1002/mrm.25450. [PubMed: 25216287]
21. Crowe ME, Larson AC, Zhang Q, Carr J, White RD, Li D, Simonetti OP. Automated rectilinear self-gated cardiac cine imaging. Magn. Reson. Med 2004;52:782–788. doi: 10.1002/mrm.20212. [PubMed: 15389958]
22. Buehrer M, Curcic J, Boesiger P, Kozerke S. Prospective self-gating for simultaneous compensation of cardiac and respiratory motion. Magn. Reson. Med 2008;60:683–690. doi: 10.1002/mrm.21697. [PubMed: 18727084]
23. Larson AC, White RD, Laub G, McVeigh ER, Li D, Simonetti OP. Self-Gated Cardiac Cine MRI. Magn. Reson. Med 2004;51:93–102. doi: 10.1002/mrm.10664. [PubMed: 14705049]
24. Han F, Rapacchi S, Hu P. Prospective cardiac motion self-gating. Quant Imaging Med Surg 2017;2:215–226. doi: 10.1186/1532-429X-15-S1-P83.
25. Bonanno G, Hays AG, Weiss RG, Schär M. Self-gated golden angle spiral cine MRI for coronary endothelial function assessment. Magn. Reson. Med 2017;00:1–11. doi: 10.1002/mrm.27060.
26. Odille F, Uribe S, Batchelor PG, Prieto C, Schaeffter T, Atkinson D. Model-based reconstruction for cardiac cine MRI without ECG or breath holding. Magn. Reson. Med 2010;63:1247–1257. doi: 10.1002/mrm.22312. [PubMed: 20432296]
27. Brau ACS, Brittain JH. Generalized self-navigated motion detection technique: Preliminary investigation in abdominal imaging. Magn. Reson. Med 2006;55:263–270. doi: 10.1002/mrm.20785. [PubMed: 16408272]
28. Larson AC, Kellman P, Arai A, Hirsch GA, McVeigh E, Li D, Simonetti OP. Preliminary investigation of respiratory self-gating for free-breathing segmented cine MRI. Magn. Reson. Med 2005;53:159–168. doi: 10.1002/mrm.20331. [PubMed: 15690515]
29. Salerno M, Sica CT, Kramer CM, Meyer CH. Optimization of spiral-based pulse sequences for first-pass myocardial perfusion imaging. Magn. Reson. Med 2011;65:1602–1610. doi: 10.1002/mrm.22746. [PubMed: 21590802]
30. Otazo R, Candès E, Sodickson DK. Low-rank plus sparse matrix decomposition for accelerated dynamic MRI with separation of background and dynamic components. Magn. Reson. Med 2015;73:1125–1136. doi: 10.1002/mrm.25240. [PubMed: 24760724]
31. Zhou R, Huang W, Yang Y, Chen X, Weller DS, Kramer CM, Kozerke S, Salerno M. Simple motion correction strategy reduces respiratory-induced motion artifacts for k-t accelerated and compressed-sensing cardiovascular magnetic resonance perfusion imaging. J. Cardiovasc. Magn. Reson 2018;20:1–13. doi: 10.1186/s12968-018-0427-1. [PubMed: 29298692]
32. Fessler JA. On NUFFT-based gridding for non-Cartesian MRI. J Magn Reson 2007;188:191–195. [PubMed: 17689121]
33. Smriti R, Stredney D, Schmalbrock P, Clymer BD. Image Registration Using Rigid Registration and Maximization of Mutual Information. In: MMVR13 (The 13th Annual Medicine Meets Virtual Reality Conference). Long Beach, CA, USA; 2005.
34. Xue Y, Yu J, Kang HS, Englander S, Rosen MA, Song HK. Automatic coil selection for streak artifact reduction in radial MRI. Magn. Reson. Med 2012;67:470–476. doi: 10.1002/mrm.23023. [PubMed: 21656562]
35. Feng L, Huang C, Shanbhogue K, Sodickson DK, Chandarana H, Otazo R. RACER-GRASP: Respiratory-weighted, aortic contrast enhancement-guided and coil-unstreaking golden-angle radial sparse MRI. Magn. Reson. Med 2017;00. doi: 10.1002/mrm.27002.
36. Pruessmann Klaas P., Weiger M, Peter B, Boesiger P. Advances in Sensitivity Encoding With Arbitrary k-Space Trajectories. Magn. Reson. Med. [Internet] 2001;651:638–651.

Author Manuscript Author Manuscript Author Manuscript Author Manuscript

37. Walsh DO, Gmitro AF, Marcellin MW. Adaptive reconstruction of phased array MR imagery. Magn. Reson. Med 2000;43:682–690. doi: 10.1002/(SICI)1522-2594(200005)43:5<682::AID-MRM10>3.0.CO;2-G. [PubMed: 10800033]
38. Lingala SG, Hu Y, DiBella E, Jacob M. Accelerated dynamic MRI exploiting sparsity and low-rank structure: k-t SLR. IEEE Trans. Med. Imaging 2011;30:1042–1054. doi: 10.1016/j.immuni.2010.12.017.Two-stage. [PubMed: 21292593]
39. Yang Y, Kramer CM, Shaw PW, Meyer CH, Salerno M. First-pass myocardial perfusion imaging with whole-heart coverage using L1-SPIRiT accelerated variable density spiral trajectories. Magn. Reson. Med 2016;76:1375–1387. doi: 10.1002/mrm.26014. [PubMed: 26538511]
40. Bland JM, Altman DG. Statistical Methods for Assessing Agreement Between Two Methods of Clinical Measurement. Lancet 1986;327:307–310. doi: 10.1016/S0140-6736(86)90837-8.
41. Rao A, Sanchez-Ortiz GI, Chandrashekara R, Lorenzo-Valdés M, Mohiaddin R, Rueckert D. Comparison of cardiac motion across subjects using non-rigid registration. Med. Image Comput. Comput. Interv. — MICCAI 2002 2002;2488:722–729. doi: 10.1007/3-540-45786-0_89.
42. Chen X, Salerno M, Yang Y, Epstein FH. Motion-compensated compressed sensing for dynamic contrast-enhanced MRI using regional spatiotemporal sparsity and region tracking: Block low-rank sparsity with motion-guidance (BLOSM). Magn. Reson. Med 2014;72:1028–1038. doi: 10.1002/mrm.25018. [PubMed: 24243528]
43. Moghari MH, Komarlu R, Annese D, Geva T, Powell AJ. Free-Breathing Steady-State Free Precession Cine Cardiac Magnetic Resonance with Respiratory Navigator Gating. Magn. Reson. Med 2015;73:1555–1561. doi: 10.1002/mrm.25275. [PubMed: 24777586]
44. Chow K, Yang Y, Shaw P, Kramer CM, Salerno M. Robust free-breathing SASHA T1mapping with high-contrast image registration. J. Cardiovasc. Magn. Reson. [Internet] 2016;18:1–14. doi: 10.1186/s12968-016-0267-9.
45. Xue H, Greiser A, Zuehlsdorff S, Jolly M-P, Guehring J, Arai AE, Kellman P. Phase-sensitive inversion recovery for myocardial T1 mapping with motion correction and parametric fitting. Magn. Reson. Med 2014;69:1408–1420. doi: 10.1002/mrm.24385.Phase-Sensitive.
46. Lustig M, Pauly JM. SPIRiT: Iterative self-consistent parallel imaging reconstruction from arbitrary k-space. Magn. Reson. Med 2010;64:457–471. doi: 10.1002/mrm.22428. [PubMed: 20665790]
47. Pruessmann KP, Weiger M, Scheidegger MB, Boesiger P. SENSE: Sensitivity encoding for fast MRI. Magn. Reson. Med 1999;42:952–962. doi: 10.1002/(SICI)1522-2594(199911)42:5<952::AID-MRM16>3.0.CO;2-S. [PubMed: 10542355]
48. Moody WE, Edwards NC, Chue CD, Taylor RJ, Ferro CJ, Townend JN, Steeds RP. Variability in cardiac MR measurement of left ventricular ejection fraction, volumes and mass in healthy adults: Defining a significant change at 1 year. Br. J. Radiol 2015;88. doi: 10.1259/bjr.20140831.
49. Malayeri AA, Johnson WC, Macedo R, Lima JAC, Bluemke DA. Cardiac Cine MRI: Quantification of the Relationship Between Fast Gradient Echo and Steady-State Free Precession for Determination of Myocardial Mass and Volumes. J Magn Reson Imaging 2008;28:60–66. doi: 10.1002/jmri.21405.Cardiac. [PubMed: 18581356]
50. Noll DC, Pauly JM, Meyer CH, Nishimura DG, Macovskj A. Deblurring for non-2D fourier transform magnetic resonance imaging. Magn. Reson. Med 1992;25:319–333. doi: 10.1002/mrm.1910250210. [PubMed: 1614315]
51. Nayak KS, Cunningham CH, Santos JM, Pauly JM. Real-Time Cardiac MRI at 3 Tesla. Magn. Reson. Med 2004;51:655–660. doi: 10.1002/mrm.20053. [PubMed: 15065236]
52. Harrison A, Adluru G, Damal K, Shaaban AM, Wilson B, Kim D, McGann C, Marrouche NF, Dibella EVR. Rapid ungated myocardial perfusion cardiovascular magnetic resonance: Preliminary diagnostic accuracy. J. Cardiovasc. Magn. Reson 2013;15:1–10. doi: 10.1186/1532-429X-15-26. [PubMed: 23324167]
53. Sudarski S, Henzler T, Dösch C, Zenge MO, Schmidt M, Nadar MS, Borggrefe M. Free-breathing Sparse Sampling Cine MR Imaging with Iterative Reconstruction for the Assessment of Left Ventricular. Radiology [Internet] 2017;282. doi: 10.1148/radiol.2016151002.

Author Manuscript Author Manuscript Author Manuscript Author Manuscript

54. Barkauskas KJ, Rajiah P, Ashwath R, Hamilton JI, Chen Y, Ma D, Wright KL, Gulani V, Griswold MA, Seiberlich N. Quantification of left ventricular functional parameter values using 3D spiral bSSFP and. J. Cardiovasc. Magn. Reson 2014:1–13. doi: 10.1186/s12968-014-0065-1.

Author Manuscript Author Manuscript Author Manuscript Author Manuscript

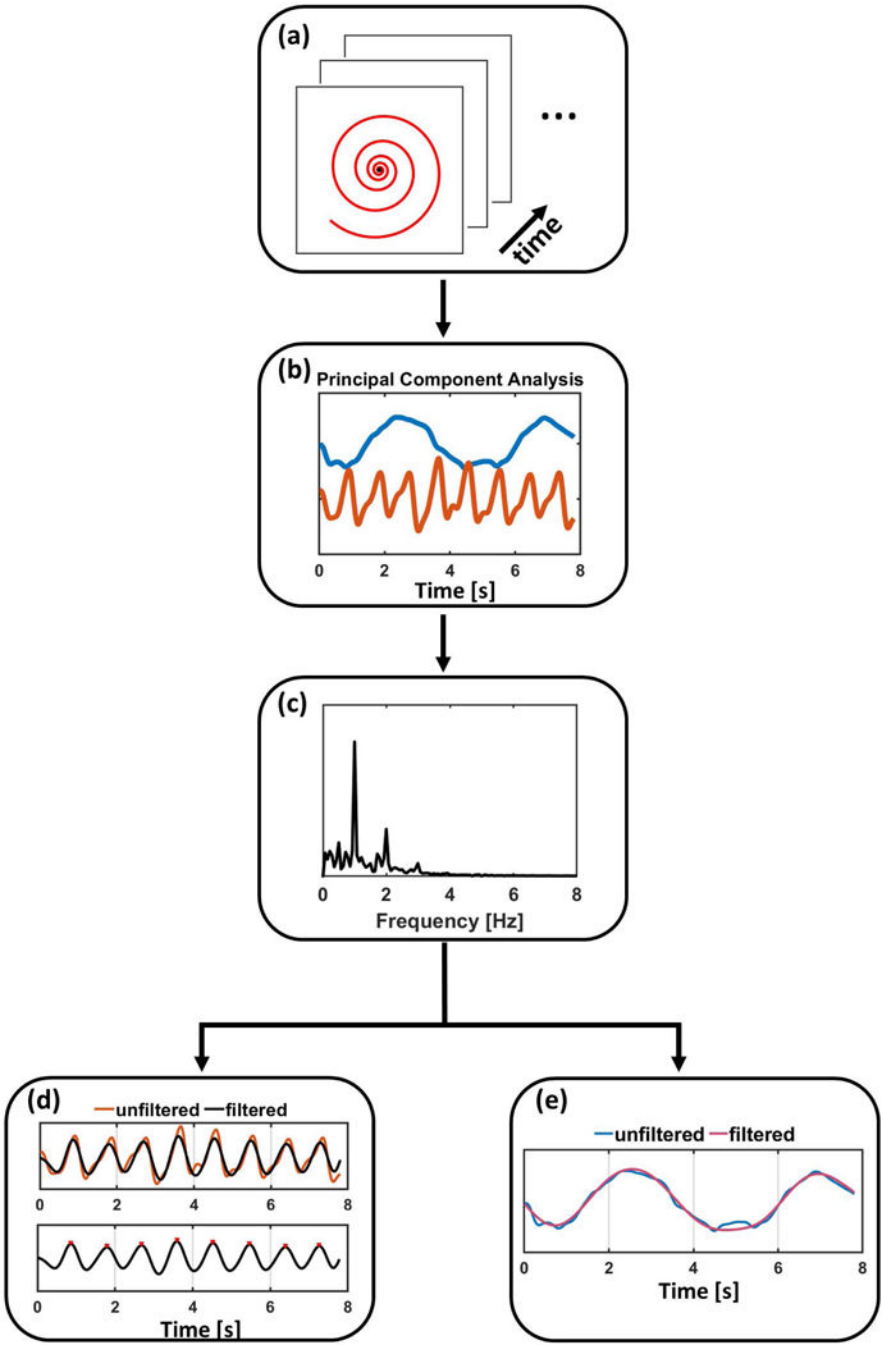

Figure 1: Pipeline of cardiac self-gating.

(a) In the first step, the 8×8 center region of *k*-space is gridded across all coils through time. (b) Principal component analysis is then performed across this data to derive temporal-basis functions. (c) Frequency spectrum analysis is performed to separate the cardiac and respiratory components. (d) Extracted filtered cardiac motion component and peak detection is performed to detect the cardiac triggers. (e) A respiratory motion component can also be derived and used for self-gating as alternative to rigid registration.

Author Manuscript Author Manuscript Author Manuscript Author Manuscript

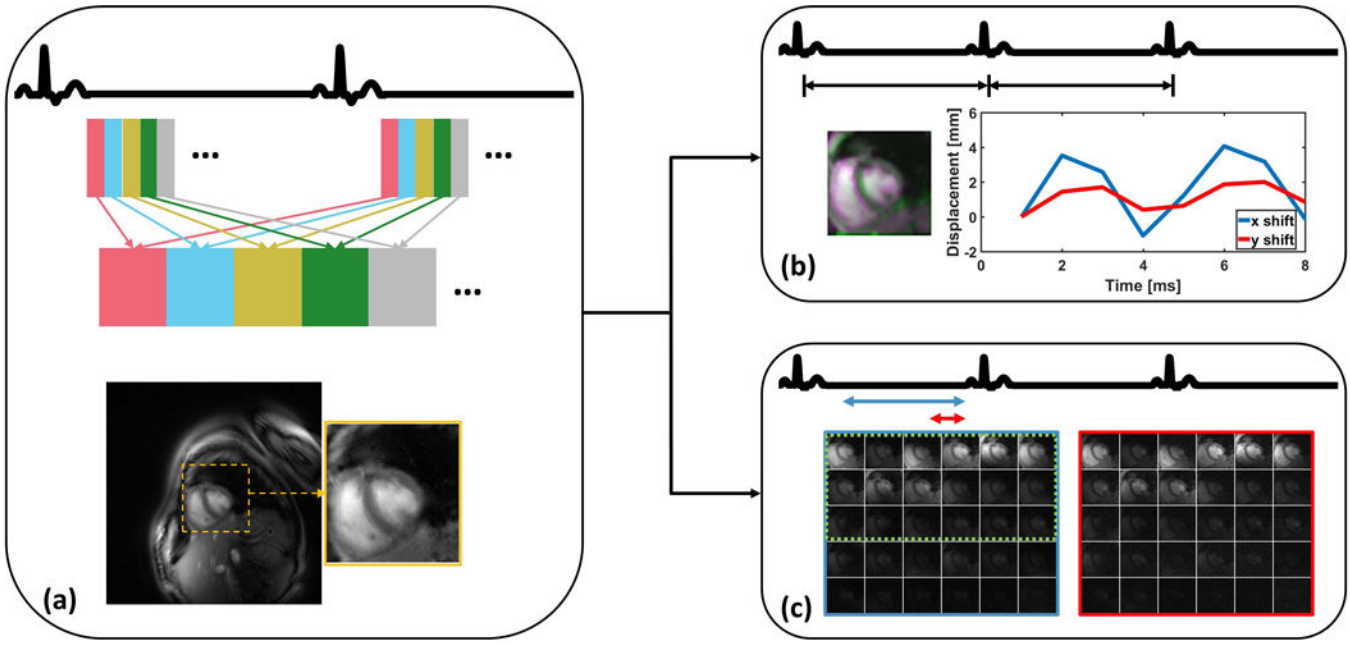

Figure 2: Pipeline of respiratory motion correction.

In the first step (a), retrospective cardiac binning of the data across multiple R-R intervals, was performed so that the heart could be located based on the variation in signal intensity due to cardiac motion throughout the cardiac cycle. Once the heart ROI was selected, further processing used only this defined ROI and data were averaged over part of individual heartbeats. In the second step (b), by using all of the spiral interleafs for each heartbeat, a single static image was created for each heartbeat and these images were registered to determine the respiratory motion. For the automatic coil selection (c), a reference image (blue) was reconstructed from a single heartbeat using a large temporal window and an aliased image (red) was reconstructed using a small temporal window. The images reconstructed from these two temporal windows provided an assessment of the artifact power, and coils with high SNR and low artifact power (circled by green dashed line) were selected appropriately.

Author Manuscript Author Manuscript Author Manuscript Author Manuscript

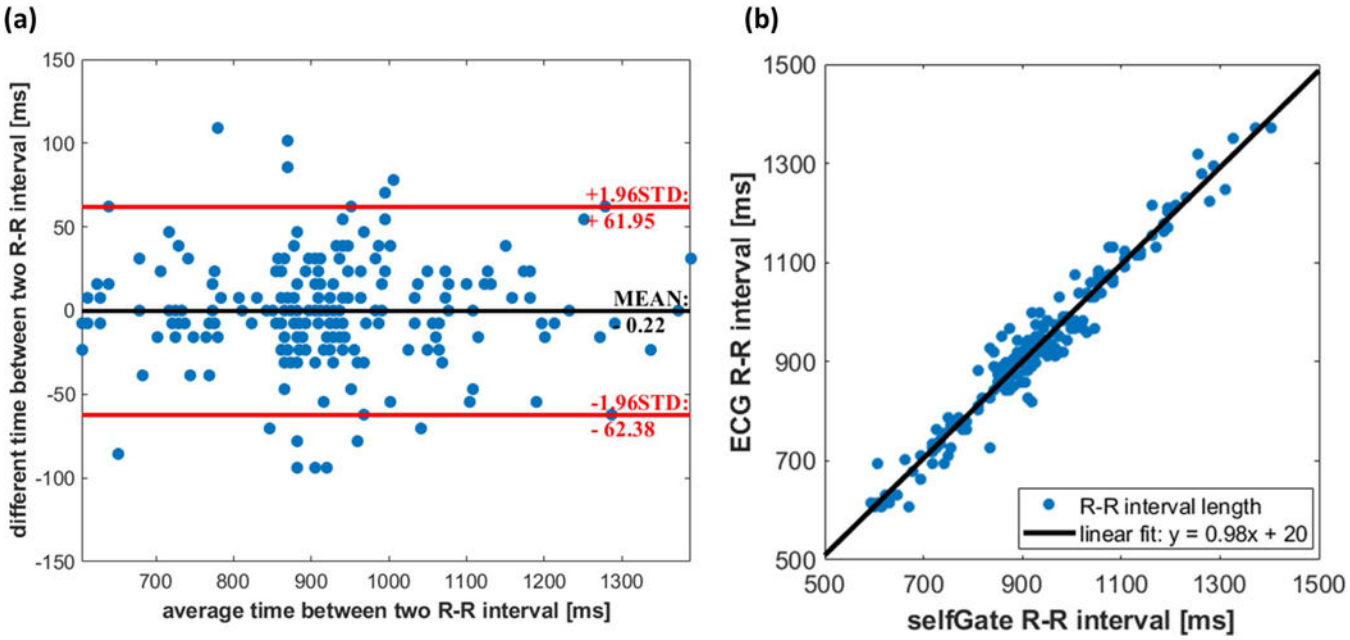

Figure 3: Cardiac gating consistency.

(a) Bland-Altman plot indicates a non-significant bias of −0.22 ms for the R-R interval length difference between self-gated signals and ECG signals across all the subjects. (b) There is a strong positive correlation relationship (R^2 = 0.96) between self-gated and ECG R-R interval lengths.

Author Manuscript Author Manuscript Author Manuscript Author Manuscript

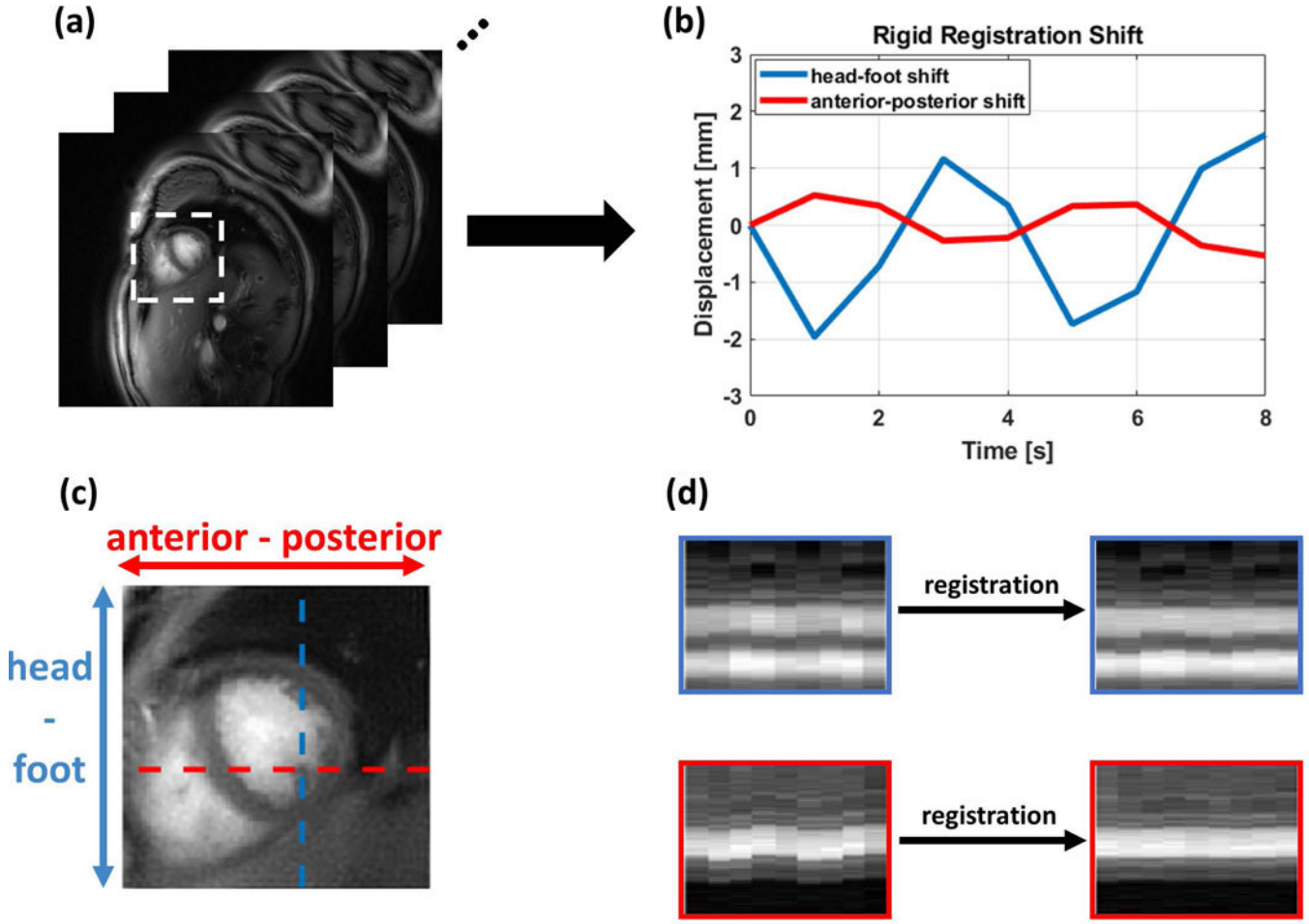

Figure 4: Motion correction performance in a representative subject.

(a) A static image was reconstructed from each heartbeat to generate the images used for respiratory motion compensation. (b) The rigid registration displacement in x (anterior-posterior: A-P) and y (head-foot: H-F) directions was determined and used to correct the respiratory position. X-t and Y-t profiles before and after registration in the H-F and A-P directions (c) are shown in (d). The heart borders are more closely aligned following respiratory motion correction.

Author Manuscript Author Manuscript Author Manuscript Author Manuscript

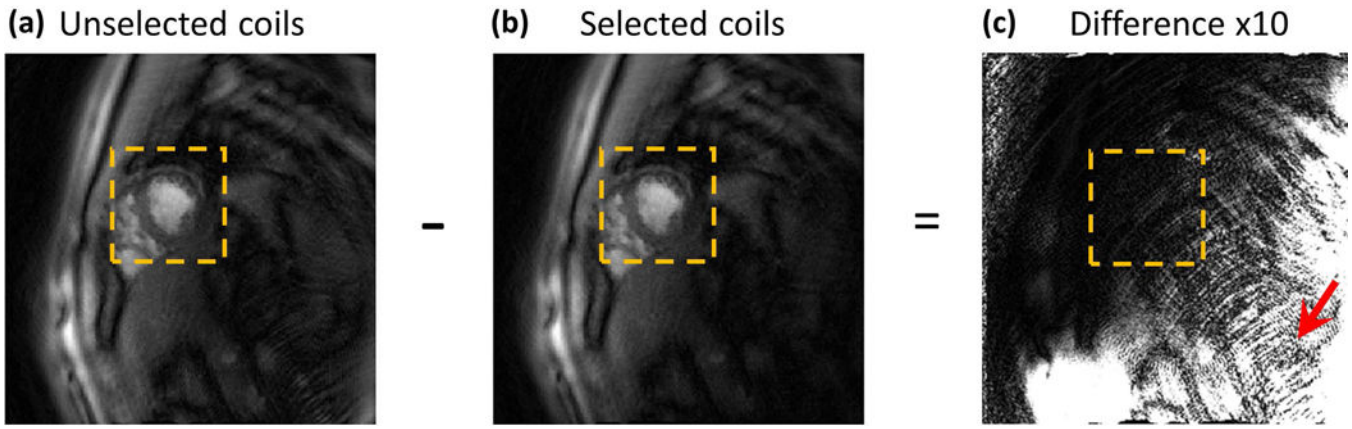

Figure 5: Automatic coil selection.

(a) and (b) show the reconstructed images before and after the proposed coil selection method, respectively. (c) is the difference image between (a) and (b), with 10-fold scaling to better visualize aliasing artifacts. The red arrow indicates aliasing caused by remote coils.

Author Manuscript Author Manuscript Author Manuscript Author Manuscript

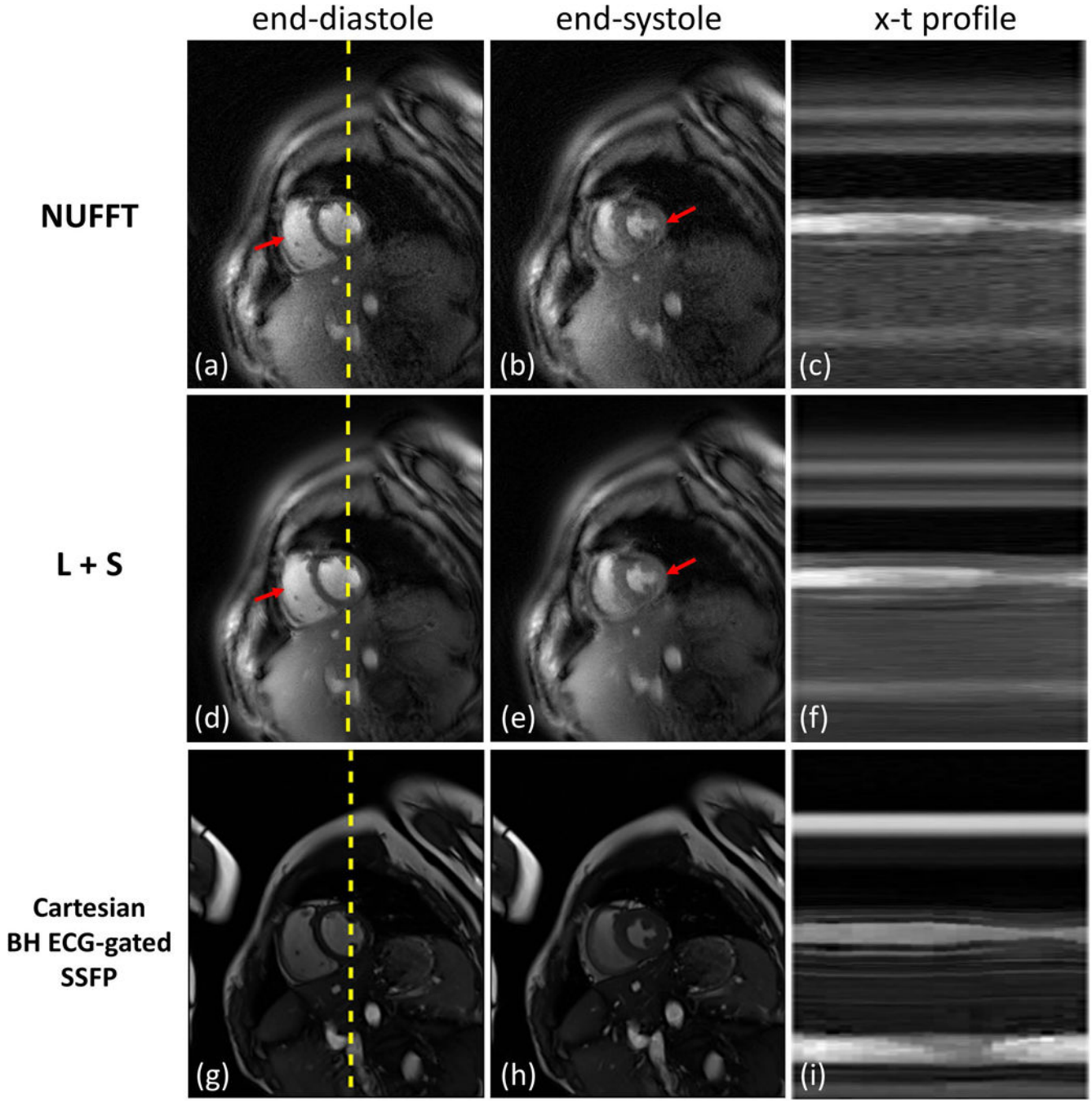

Figure 6: Short axis SPARCS images from a healthy volunteer.

The first and second rows show SPARCS reconstructed images using NUFFT and L+S, respectively. The third row shows the clinically used breath-hold ECG-gated bSSFP images for comparison. End diastolic and end systolic images are shown in the first and second columns, respectively, and x-t profiles are shown in the last column. X positions are indicated as dashed yellow lines in end-diastolic images. Red arrows indicate aliasing artifacts that are obvious in NUFFT images but are reduced by the L+S technique. The image-quality scores for this subject from 2 cardiologists were: 4 and 3 for SPARCS NUFFT

images; 5 and 4.5 for SPARCS L+S images; and 5 and 5 for breath-hold ECG-gated bSSFP images.

Author Manuscript Author Manuscript Author Manuscript Author Manuscript

Author Manuscript Author Manuscript Author Manuscript Author Manuscript

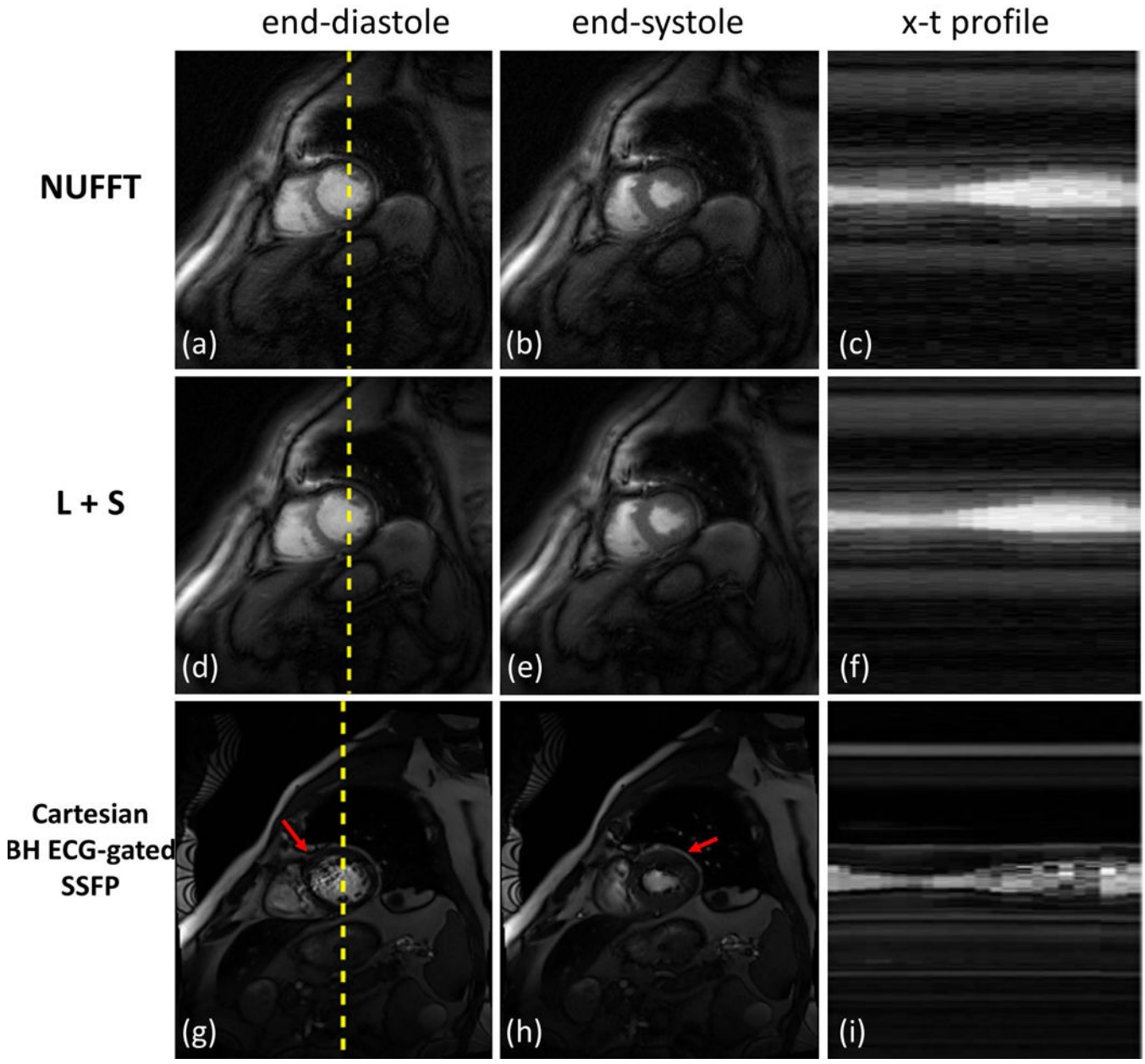

Figure 7: Short axis SPARCS images from a clinical patient subject.

The first and second rows show SPARCS reconstructed images using NUFFT and L+S, respectively. The third row shows the clinically used breath-hold ECG-gated bSSFP images for comparison. End-diastolic and end-systolic images are shown in the first and second columns, respectively, and x-t profiles are shown in the last column. X positions are indicated as dashed yellow lines in end-diastolic images. Red arrows indicate susceptibility artifacts that often occur in clinical bSSFP images. The image-quality scores for this subject from 2 cardiologists were: 4 and 3.5 for SPARCS NUFFT images; 5 and 4.5 for SPARCS L +S images; and 3 and 3.5 for breath-hold ECG-gated bSSFP images.

Author Manuscript Author Manuscript Author Manuscript Author Manuscript

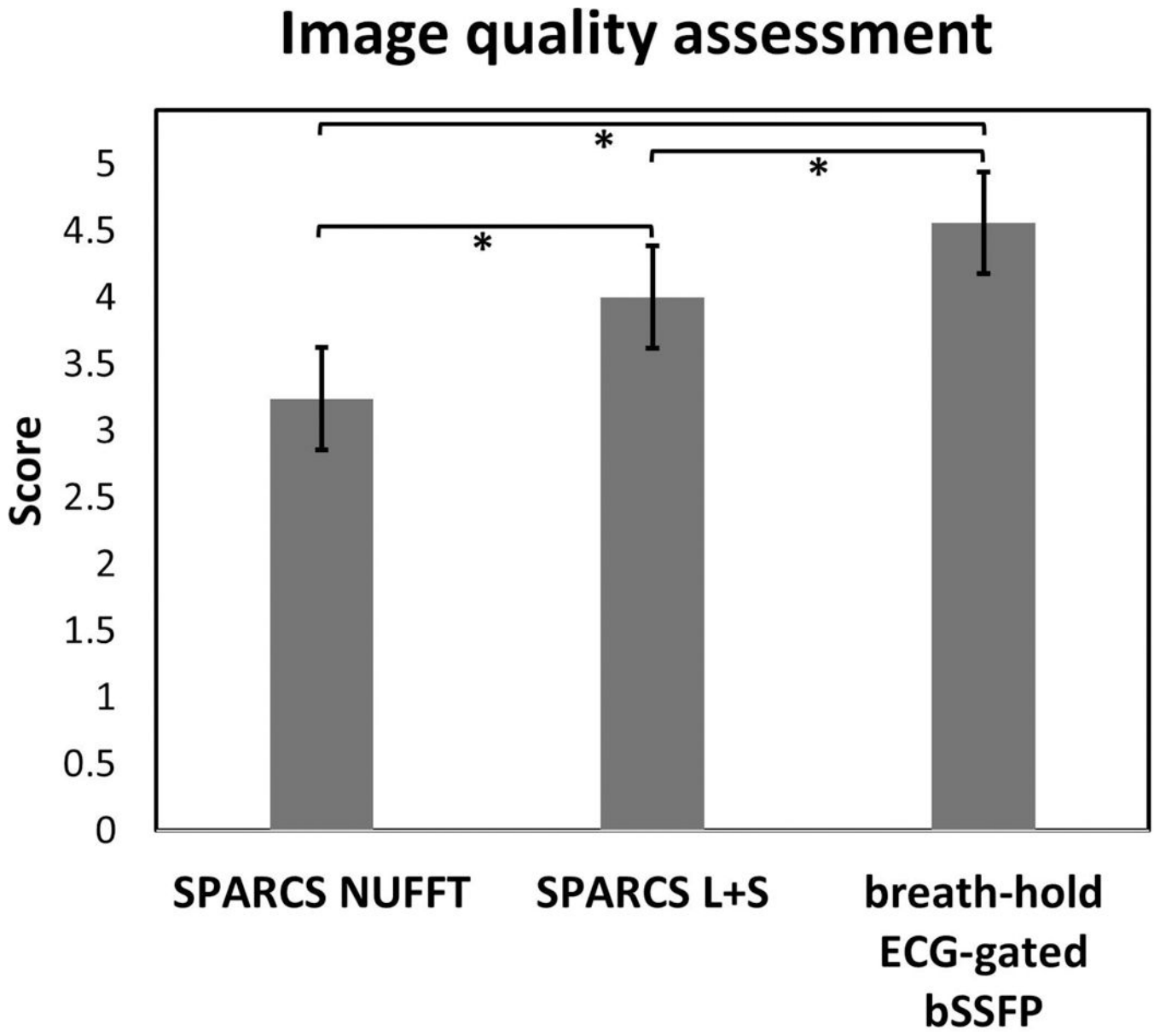

Figure 8: Blinded image quality scores for all subjects.

The bar plot shows the scores for SPARCS images using NUFFT and L+S, as well as breath-hold ECG-gated bSSFP images, graded in a blinded fashion by 2 cardiologists. * indicates a significant difference ($p < 0.001$).

Author Manuscript Author Manuscript Author Manuscript Author Manuscript

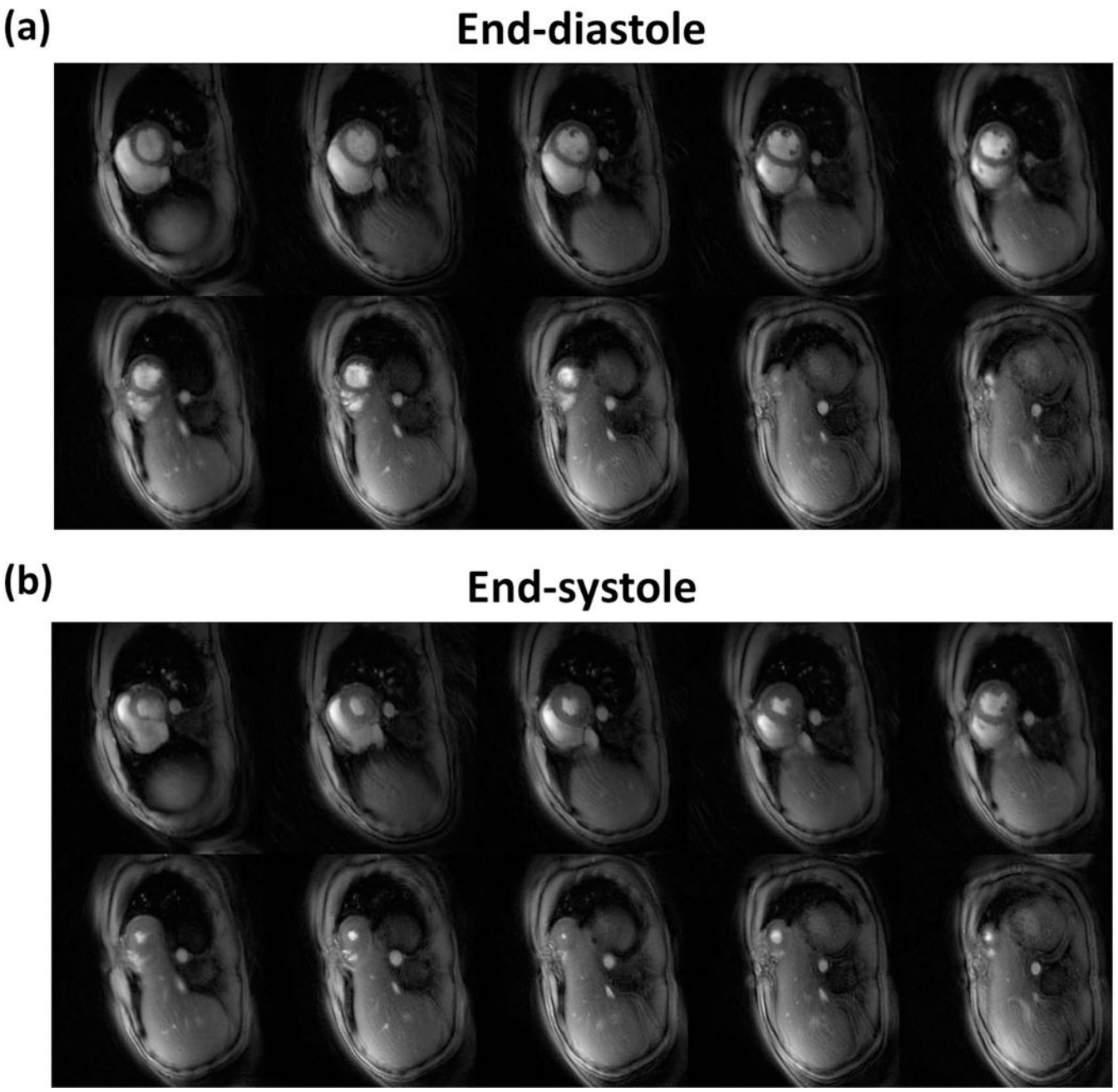

Figure 9: Whole-heart reconstruction results.

(a) The top 2 rows of images are L+S diastolic frames across all slices. (b) The bottom 2 rows of images are L+S systolic frames across all slices.

Author Manuscript Author Manuscript Author Manuscript Author Manuscript

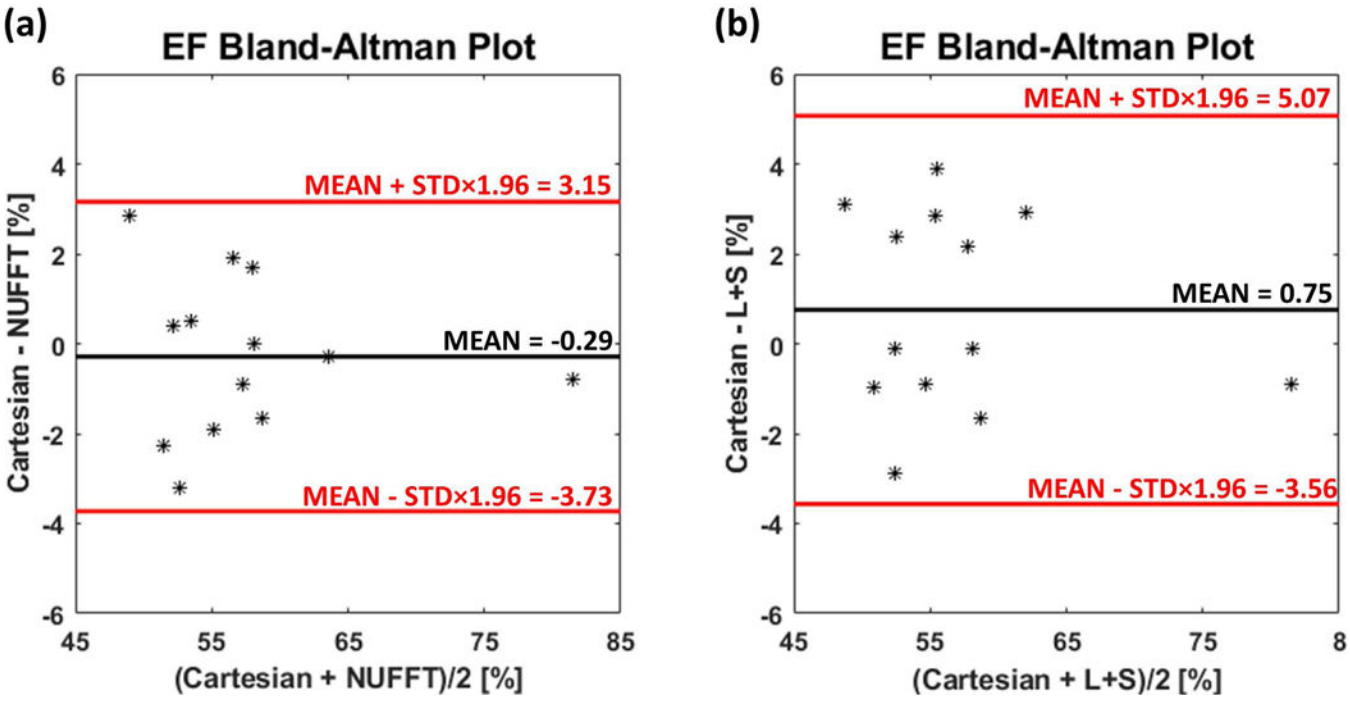

Figure 10: Bland-Altman plots of EF for the subjects with whole-heart coverage.

(a) Bland-Altman plot of EF calculated from Cartesian bSSFP image results (Cartesian) and SPARCS NUFFT image results (NUFFT). (b) Bland-Altman plot of EF calculated from Cartesian bSSFP image results and SPARCS L+S image results (L+S).